
Data-Limited Tissue Segmentation using Inpainting-Based Self-Supervised Learning

Jeffrey Dominic
Department of Radiology
Stanford University

Nandita Bhaskhar
Department of Electrical Engineering
Stanford University

Arjun D. Desai
Department of Radiology
Department of Electrical Engineering
Stanford University

Andrew Schmidt
Department of Radiology
Stanford University

Elka Rubin
Department of Radiology
Stanford University

Beliz Gunel
Department of Radiology
Department of Electrical Engineering
Stanford University

Garry E. Gold
Department of Radiology
Stanford University

Brian A. Hargreaves
Department of Radiology
Department of Electrical Engineering
Department of Bioengineering
Stanford University

Leon Lenchik
Department of Radiology
Wake Forest School of Medicine

Robert Boutin
Department of Radiology
Stanford University

Akshay S. Chaudhari
Department of Radiology
Department of Biomedical Data Science
Stanford Cardiovascular Institute
Stanford University

Abstract

Purpose To evaluate the efficacy of two self-supervised learning (SSL) methods (inpainting-based pretext tasks of context prediction and context restoration) for medical image segmentation in label-limited scenarios, and to investigate the effect of implementation design choices for SSL on downstream segmentation performance.

Methods Manual segmentation labels were created for 3D knee MRI and 2D abdominal CT datasets. Multiple versions of self-supervised U-Net models were trained to segment tissues in both datasets, each using a different combination of design choices and pretext tasks to determine the effect of different design choices on segmentation performance. The combination of these design choices that resulted in the most significant improvement in Dice score over supervised learning for both datasets was used to train an optimally trained model for segmentation. This model was pretrained on different amounts of unlabeled data to determine the effect of pretraining dataset size on segmentation performance. The highest performing models from this experiment were compared with baseline supervised models for computing clinically-relevant metrics in label-limited scenarios.

Results SSL pretraining with context restoration using 32x32 patches and Poission-disc sampling, transferring only the pretrained encoder weights, and fine-tuning immediately with an initial learning rate of 1e-3 provided the most benefit over supervised learning for MRI and CT tissue segmentation accuracy ($p < 0.001$). For both datasets and most label-limited scenarios, pretraining using the maximum amount of unlabeled images resulted in better segmentation performance than pretraining using only the training set ($p < 0.05$). SSL models pretrained with this amount of data also outperformed baseline supervised models in the computation of clinically-relevant metrics in scenarios with very low amounts of labeled data, especially for challenging classes to segment such as intramuscular adipose tissue on CT images and patellar cartilage on MR images.

Conclusion We demonstrate how SSL can overcome paucity of labels for improving tissue segmentation by using unlabeled datasets.

1 Introduction

Segmentation is an essential task in medical imaging that is common across different imaging modalities and fields such as cardiac, abdominal, and musculoskeletal imaging, amongst others [1, 2, 3]. Deep learning (DL) has enabled high performance on these challenges, but the power-law relationship between algorithmic performance and the amount of high-quality labeled training data fundamentally limits robustness and widespread use [4].

Recent advances in self-supervised learning (SSL) provide an opportunity to reduce the annotation burden for deep learning models. In SSL, a model is first pretrained on a “pretext” task, during which unlabeled images are perturbed and the model is trained to predict or correct the perturbations. The model is then fine-tuned for downstream tasks. Previous works have shown that such models can achieve high performance even when fine-tuned on only a small labeled training set [5, 6, 7]. While most SSL models in computer vision have been used for the downstream task of image classification, segmentation comparatively remains an under-explored task [8].

In this work, we systematically evaluate the efficacy of SSL for medical image segmentation across two domains – MRI and CT. We investigate “context prediction” [5] and “context restoration” [6], two well-known and easy-to-implement archetypes of restoration-based pretext tasks that produce image-level representations during pretraining for eventual fine-tuning. Context prediction sets pixel values in random image patches to zero, while context restoration randomly swaps pairs of image patches within an image while maintaining the distribution of pixel values (Figure 1). For both tasks, the model needs to recover the original image given the corrupted image, a process we refer to as “inpainting”. We consider these two tasks because they maintain same input-output sizes, akin

to segmentation. We hypothesize that such pretext tasks allow construction of useful, image-level representations that are more suitable for downstream segmentation.

While context prediction and context restoration have been proposed before, the effects of the large space of design choices for these two pretext tasks, such as patch sizes for image corruption and learning rates for transfer learning, are unexplored. In addition, prior works exploring SSL for medical image segmentation have primarily focused on the accuracy of segmentation using metrics such as Dice scores [6, 9], but have not investigated if SSL can improve clinically-relevant metrics, such as T2 relaxation times for musculoskeletal MRI scans and mean Hounsfield Unit (HU) values for CT scans. These metrics can provide biomarkers of biochemical changes in tissue structure prior to the onset of gross morphological changes [10, 11]. Furthermore, within the context of empirical data scaling laws in DL, past SSL works have rarely explored benefits of increasing the number of unlabeled images during pretraining [12]. Characterizing the efficiency of SSL methods with unlabeled data can lead to more informed decisions regarding data collection, an important practical consideration for medical image segmentation. In this work, we address the above gaps by

- (1) investigating how different design choices in SSL implementation affect the quality of the pretrained model,
- (2) calculating how varying unlabeled data extents affects SSL performance for downstream segmentation,
- (3) quantifying our results using clinically-relevant metrics to investigate if SSL can outperform supervised learning in label-limited scenarios,
- (4) evaluating where SSL can improve performance, across different extents of labeled training data availability, and
- (5) providing detailed analyses, recommendations, and open-sourcing our code to build optimal SSL models for medical image segmentation.

2 Materials and Methods

2.1 Datasets

2.1.1 MRI Dataset

We used 155 labeled knee 3D MRI volumes (around 160 slices per volume) from the SKM-TEA dataset [13] and 86 unlabeled volumes (around 160 to 180 slices per volume), each with slice dimensions of 512x512 (other scan parameters in [13]). All volumes were acquired using a 5-minute 3D quantitative double-echo in steady-state (qDESS) sequence, which has been used for determining morphological and quantitative osteoarthritis biomarkers and for routine diagnostic knee MRI [14, 15, 16, 17]. The labeled volumes included manual segmentations for the femoral, tibial, and patellar cartilages, and the meniscus. The labeled volumes were split into 86 volumes for training, 33 for validation, and 36 for testing, following the splits prescribed in [13]. The 86 training volumes were further split into additional subsets, consisting of 50% (43 volumes), 25% (22 volumes), 10% (9 volumes), and 5% (5 volumes) training data, to represent label-limited scenarios. All scans in smaller subsets were included in larger subsets.

2.1.2 CT Dataset

The 2D CT dataset consisted of 886 labeled and 7799 unlabeled abdominal CT slices at the L3 vertebral level. The unlabeled images were used in a prior study exploring the impact of body composition on cardiovascular outcomes [18]. The labeled slices included manual segmentations for subcutaneous, visceral, and intramuscular adipose tissue and muscle. These labeled slices were split into 709 slices for training, 133 for validation, and 44 for testing. The training set was split in a similar manner as the MRI volumes into 4 additional subsets of 50% (354 slices), 25% (177 slices), 10% (71 slices), and 5% (35 slices) training data. No metadata from the dataset was used in any models.

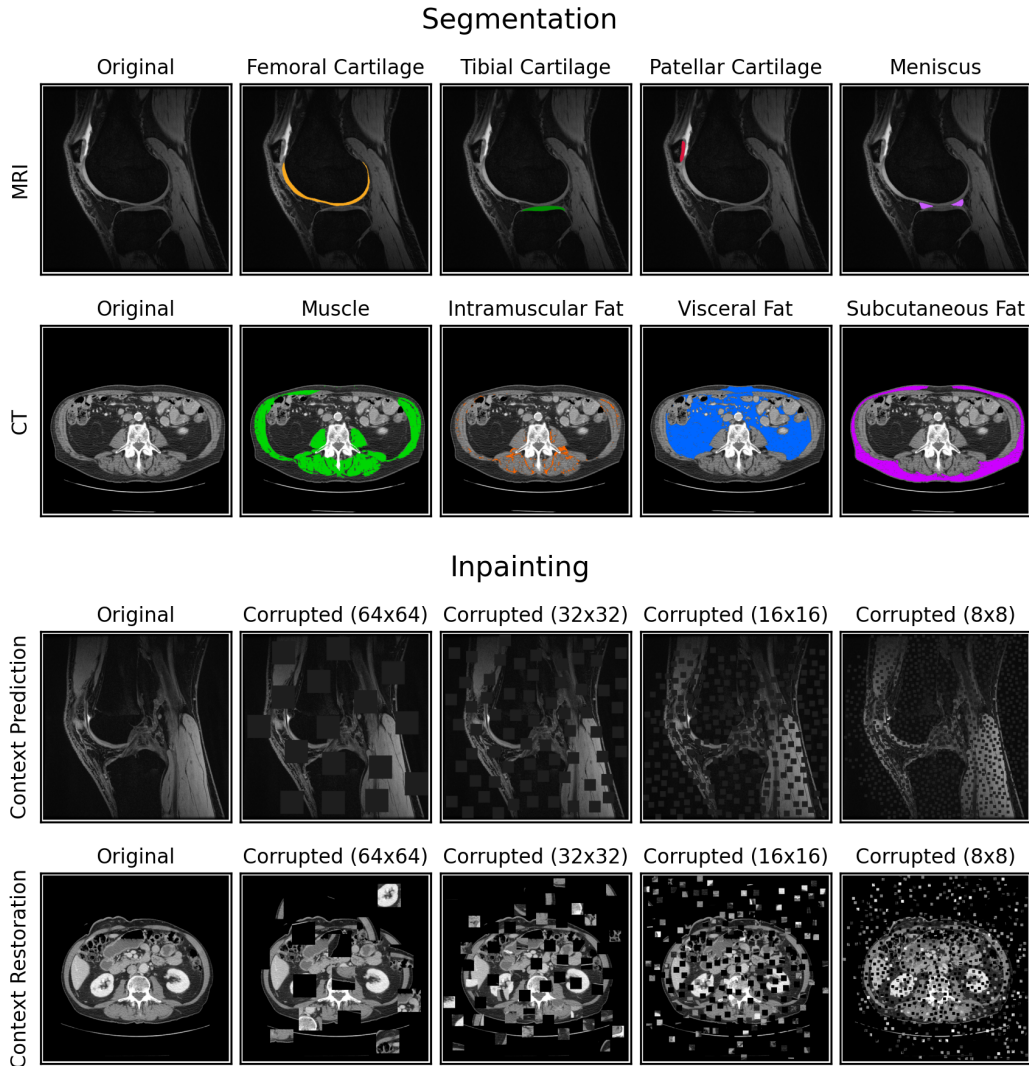


Figure 1: Example ground truth segmentations for the MRI and CT datasets (both with dimensions 512x512), and example image corruptions for context prediction (zero-ing image patches) and context restoration (swapping image patches). Since image corruption happens after normalization, the zeroed out image patches for context prediction were actually replaced with the mean of the image. The “Inpainting” section depicts image corruptions with four different patch sizes: 64x64, 32x32, 16x16, and 8x8. The locations of these patches were determined using Poisson-disc sampling to prevent randomly overlapping patches.

2.2 Data Preprocessing

All models segmented 2D slices for MRI and CT images. Each CT image was preprocessed at different windows and levels (W/L) of HU to emphasize different image contrasts, resulting in three-channel images: soft-tissue (W/L=400/50), bone (W/L=1800/40), and a custom setting (W/L=500/50). All images were normalized to have zero mean and unit standard deviation, with MR images normalized by volume and CT images normalized per channel.

2.3 Model Architecture and Optimization

2D U-Net models [19] with Group Normalization [20], weight standardization [21], and He random weight initializations [22] were used for inpainting and segmentation (Figure 2). Both inpainting and

Table 1: Demographics of the subjects included in this study. Age is shown as mean \pm standard deviation. For the CT dataset, one subject did not have age information and four subjects did not have gender information.

MRI			
Split	Gender	# Volumes (# Slices)	Age (range)
Train	Male	46 (7360)	44.7 \pm 17.7 (17 - 75)
	Female	40 (6400)	42.9 \pm 18.5 (16 - 87)
	Total	86 (13760)	43.9 \pm 18.1 (16 - 87)
Validation	Male	18 (2880)	37.3 \pm 16.8 (18 - 68)
	Female	15 (2400)	53.2 \pm 14.9 (18 - 79)
	Total	33 (5280)	44.5 \pm 17.8 (18 - 79)
Test	Male	26 (4156)	37.9 \pm 14.9 (18 - 71)
	Female	10 (1584)	53.0 \pm 11.9 (31 - 73)
	Total	36 (5740)	42.1 \pm 15.6 (18 - 73)
Unlabeled	Male	37 (5446)	38.1 \pm 16.9 (15 - 77)
	Female	49 (6686)	52.1 \pm 18.5 (14 - 97)
	Total	86 (12132)	46.1 \pm 19.1 (14 - 97)
CT			
Split	Gender	# Slices	Age (range)
Train	Male	362	68.2 \pm 11.4 (20 - 97)
	Female	343	71.1 \pm 10.5 (18 - 95)
	Total	709	69.6 \pm 11.1 (18 - 97)
Validation	Male	63	69.1 \pm 9.5 (32 - 83)
	Female	69	71.0 \pm 11.0 (32 - 89)
	Total	133	70.1 \pm 10.4 (32 - 89)
Test	Male	18	70.6 \pm 11.9 (47 - 92)
	Female	26	73.1 \pm 11.7 (44 - 93)
	Total	44	72.1 \pm 11.9 (44 - 93)
Unlabeled	Male	3167	51.5 \pm 17.1 (18 - 101)
	Female	4632	51.6 \pm 17.1 (18 - 100)
	Total	7799	51.6 \pm 17.1 (18 - 101)

segmentation used identical U-Nets, except for the final convolutional layer, which we refer to as the “post-processing” layer. For inpainting, the post-processing layer produced an output image with the same number of channels as the input image, whereas for segmentation, it produced a 4-channel image for the four segmentation classes in each dataset.

We used L2 norm loss for inpainting and Dice loss, aggregated over mini-batches per segmentation class, for segmentation. All training was performed with early stopping and the ADAM optimizer [23] ($\beta_1=0.99$ and $\beta_2=0.995$) with a batch size of 9 on an NVIDIA 2080Ti GPU. Additional details are in the Supplementary Material (Section 6.1.1).

2.4 Image Corruption for Pretext Tasks

We incorporated random block selection to select square image patches during pretraining. For context prediction, we set randomly selected patches of dimensions $K \times K$ to zero until they formed at least 1/4th of the total image area. For context restoration, randomly selected pairs of non-overlapping $K \times K$ image patches were swapped in an iterative manner until the number of corrupted pixels was at least 1/4th the total image area. We refer to the result of both methods as “masks”. The context prediction binary mask specified which pixels were zero and the context restoration mask was a list of patch pairs to be swapped. When pretraining with multi-channel CT images, the locations of the

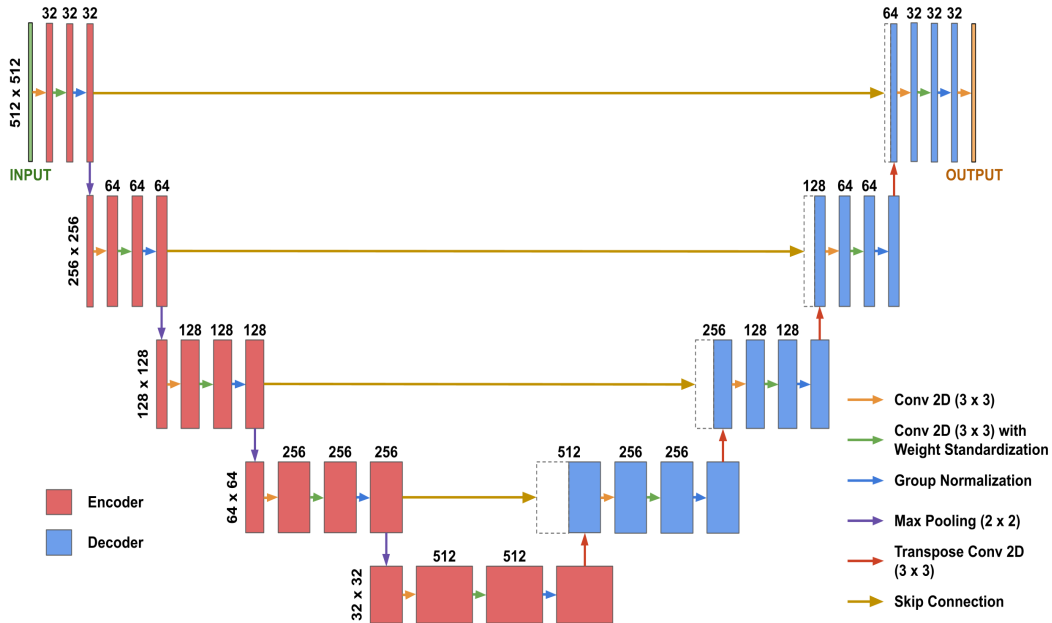


Figure 2: The U-Net architecture used for both inpainting and segmentation, which includes layers grouped into three categories: the “encoder” (in red), the “decoder” (in blue), and the “post-processing” layer (the final convolutional layer). Each dotted rectangular box represents a feature map from the encoder that was concatenated to the first feature map in the decoder at the same level.

patch corruptions were identical across channels to avoid shortcut learning [24]. Example image corruptions are shown in Figure 1.

To train the model to inpaint any arbitrarily corrupted image region without memorization of image content, we sampled a random mask every iteration for all images. For computational efficiency, we precomputed 100 random masks before training. We further randomly rotated the masks by either 0, 90, 180, or 270° counter-clockwise to increase the effective number of masks used during training to 400.

2.5 Design Choices for SSL Implementation

Design choices for inpainting-based SSL segmentation revolving around pretraining task implementations [5, 6] and transfer learning [25, 26, 27] have not been systematically compared. To overcome these shortcomings, we explored the following questions:

1. Which pretrained weights should be transferred for fine-tuning?
2. How should the transferred pretrained weights be fine-tuned?
3. What should be the initial learning rate when fine-tuning?
4. What patch size should be used when corrupting images for inpainting?
5. How should the locations of the patches be sampled when corrupting images for inpainting?

2.5.1 Design Choices for Transfer Learning (#1-3)

For design choice #1 (which pretrained weights to transfer), we compared transferring only the U-Net encoder weights [5] with transferring both the encoder and decoder weights [6].

For design choice #2, we compare (i) fine-tuning all pretrained weights immediately after transferring [25, 26], and (ii) freezing pretrained weights after transferring and training until convergence, then subsequently unfreezing pretrained weights and training all weights until convergence [27, 28].

For design choice #3, we selected four initial learning rates: 1e-2, 1e-3, 1e-4, and 1e-5, to evaluate whether pretrained features are distorted with larger learning rates.

To compare different combinations of these three design choices, we performed a grid search and defined the best combination to be the one with the best segmentation performance on the MRI test set when trained with the MRI training subset with 5% training data. More details are in the Supplementary Material (Section 6.2.1).

2.5.2 Design Choices for Pretraining (#4-5)

For design choice #4, we compare patch sizes of 64x64, 32x32, 16x16, and 8x8 (Figure 1).

For design choice #5, we compare two sampling methods: i) fully-random sampling where the location of each patch was selected at random and constrained to lie completely within the image [5, 6], and (ii) Poisson-disc sampling that enforces the centers of all $K \times K$ patches to lie at least $K\sqrt{2}$ pixels away from each other to prevent overlapping patches [29].

To compare different combinations of design choices #4 and #5 and the two pretext tasks, we performed a grid search by training a model for each combination five times, each time using one of the five training data subsets, for both datasets. We also trained a fully supervised model for each dataset and training data subset for a baseline comparison.

All models were fine-tuned in an identical manner with the same random seed after pretraining, using the best combination of design choices #1-3. All inpainting models were compared by computing the L2 norm of the generated inpainted images. All segmentation models were compared by computing the Dice coefficient for each segmentation class in the test set, averaged across all available volumes/slices.

2.5.3 Optimal Pretraining Evaluation

We defined the optimal pretraining strategy as the strategy that provided the most benefit over supervised learning, across image modalities and training data extents, in the experiment described in Section 2.5.2.

For each baseline (fully supervised model) and SSL model trained in the experiment using 50%, 25%, 10%, and 5% training data, we computed class-averaged Dice scores for every test volume/slice in the MRI and CT datasets. For each pretraining strategy and dataset, we compared whether the set of Dice scores of the corresponding SSL models were significantly higher than that of the respective fully-supervised models using one-sided Wilcoxon signed-rank tests. As a heuristic, the pretraining strategies were sorted by their associated p-values and the pretraining strategy that appeared in the top three for both the MRI and CT datasets was selected as the optimal pretraining strategy. We defined the optimally trained model for each dataset as the SSL model that was pretrained with this optimal pretraining strategy and fine-tuned for segmentation using the best combination of design choices #1-3.

2.6 Impact of Extent of Unlabeled Data

To measure the effect of the number of pretraining images on downstream segmentation performance, the optimally trained model was pretrained with the standard training set as well as two supersets of the training set containing additional unlabeled imaging data. We refer to the standard training set as 100% pretraining data (86 volumes for MRI and 709 slices for CT). For the MRI dataset, the second and third sets consisted of 150% (129 volumes) and 200% (172 volumes) pretraining data, respectively. For the CT dataset, the second and third sets consisted of 650% (4608 slices) and 1200% (8508 slices) pretraining data, respectively. After pretraining, all the pretrained models were fine-tuned with the five subsets of labeled training data and a Dice score was computed for each fine-tuned model, averaged across all segmentation classes and all volumes/slices in the test set.

For MRI and CT, the pretraining dataset that led to the best average Dice score across the extents of labeled training data was chosen for further experiments.

2.7 Comparing SSL and Fully-Supervised Learning

We compared baseline fully-supervised models and the optimally trained models pretrained with the chosen pretraining dataset from the experiment described in Section 2.6. For each training data subset, models were evaluated using two clinically-relevant metrics for determining cartilage, muscle, and adipose tissue health status. For MRI, we computed mean T2 relaxation time per tissue and tissue volume [30]. For CT, we computed cross-sectional area and mean HU value per tissue. We calculated their percentage errors by comparing them to values derived from using ground truth segmentations to compute the metrics.

2.8 Statistical Analysis

All statistical comparisons were computed using one-sided Wilcoxon signed-rank tests. All statistical analyses were performed using the SciPy (v1.5.2) library [31], with Type-1 $\alpha = 0.05$.

3 Results

The subject demographics of all labeled and unlabeled volumes/slices are shown in Table 1.

3.1 Design Choices for Transfer Learning

We observed that all pretrained model variants had high performance when first fine-tuned with an initial learning rate of $1e-3$ and then fine-tuned a second time with an initial learning rate of $1e-4$. Transferring pretrained encoder weights only and fine-tuning once immediately with an initial learning rate of $1e-3$ achieved similar performance, with the added benefit of reduced training time. Consequently, we used these as the best combination of the three design choices for transfer learning. Additional details are in the Supplementary Material (Section 6.2.2).

3.2 Design Choices for Pretraining

The L2 norm consistently decreased as a function of patch size for all combinations of pretext tasks (context prediction and context restoration) and sampling methods (random and Poisson-disc) (Table 2). Furthermore, L2 norms for Poisson-disc sampling were significantly lower than those for random sampling ($p < 0.05$). For all combinations, inpainted MRI images were of higher quality than inpainted CT images.

Dice scores for fully supervised baselines ranged from 0.67-0.88 across subsets of training data for MRI images. Downstream segmentation performance for the MRI dataset was similar for all combinations of pretext task, patch size, and sampling method (Figure 3). All SSL models matched (within 0.01) or outperformed the fully supervised model in low-label regimes with 25% training data or less for the femoral cartilage, patellar cartilage, and meniscus, and had comparable performance for higher data extents. For the tibial cartilage, all SSL models outperformed the fully supervised model when trained on 5% training data and had comparable performance for higher data extents. The difference in Dice score between each self-supervised model and the fully supervised model generally increased as the amount of labeled training data decreased. SSL pretraining also enabled some models to outperform the fully supervised model trained with 100% training data in patellar cartilage segmentation.

Dice scores for fully supervised baselines were consistently higher for CT images than for MRI images, with the exception of intramuscular adipose tissue. Unlike with the MRI dataset, downstream SSL segmentation for CT in low-label regimes depended on the pretext task and the patch size used during pretraining (Figure 4). Models pretrained with larger patch sizes (64x64; 32x32) often outperformed those pretrained with smaller patch sizes (16x16; 8x8) for muscle, visceral fat, and subcutaneous fat segmentation, when trained with either 5% or 10% labeled data. Furthermore, when 25% training data or less was used, models pretrained with 32x32 patches using context restoration almost always outperformed fully supervised models for muscle, visceral fat, and subcutaneous fat segmentation, but rarely did so when pretrained using context prediction. For intramuscular fat, all SSL models had comparable performance with fully supervised models in low-label regimes. For high-label regimes (over 25% labeled data), all SSL models had comparable performance with fully supervised models for all four segmentation classes.

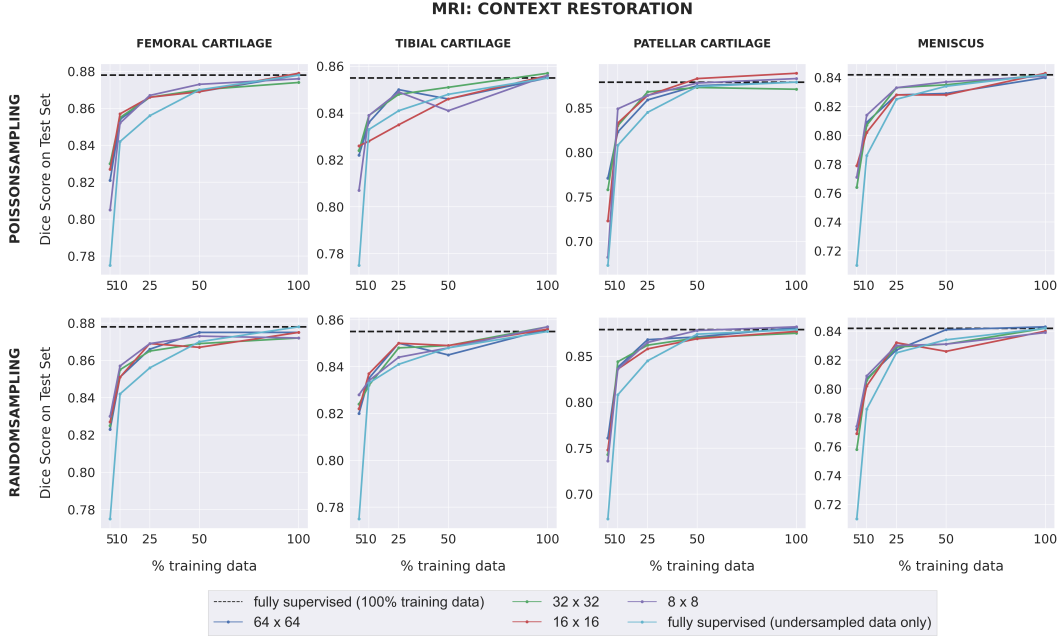


Figure 3: The downstream segmentation performance on the MRI dataset for the Context Restoration pretext task as measured by the Dice score for every combination of patch size and sampling method used during pretraining, evaluated in five different scenarios of training data availability. In each scenario, every model is trained for segmentation using one of the five different subsets of training data as described in Section 2.1.1. The black dotted line in each plot indicates the performance of a fully supervised model trained using all available training images. The light blue curve indicates the performance of a fully supervised model when trained using each of the five different subsets of training data. Similar plots for the Context Prediction pretext task are given in the Supplementary Section.

3.3 Optimal Pretraining Evaluation

The top 5 pretraining strategies for the MRI dataset and the top 3 pretraining strategies for the CT dataset led to significantly better segmentation performance compared to fully supervised learning ($p < 0.001$) (Table 3).

For MRI, the top 5 strategies all consisted of pretraining with context restoration, with minimal differences in p-value based on the patch size and sampling method used. For CT, the top 5 strategies used a patch size of at least 32×32 during pretraining. The strategy of pretraining with context restoration, 32×32 patches, and Poisson-disc sampling was in the top 3 for both datasets, and was therefore selected as the optimal pretraining strategy.

3.4 Impact of Extent of Unlabeled Data

For both datasets and for most subsets of labeled training data used during fine-tuning (except 25% and 10% labeled training data for MRI), the optimally trained model performed significantly better in downstream segmentation when pretrained on the maximum amount of data per dataset (200% pretraining data for MRI and 1200% pretraining data for CT) than when pretrained on only the training set ($p < 0.05$). When 25% or 10% labeled training data was used for MRI segmentation, the optimally trained model achieved a higher mean Dice score when pretrained on 200% pretraining data, but this was not statistically significant ($p = 0.3$ for 25% labeled training data and $p = 0.02$ for 10% labeled training data).

For MRI, Dice scores almost always improved as the amount of pretraining data increased. This improvement was greatest when only 5% of the labeled training data was used for training segmentation. Improvements in segmentation performance were slightly higher for CT. For all extents of labeled

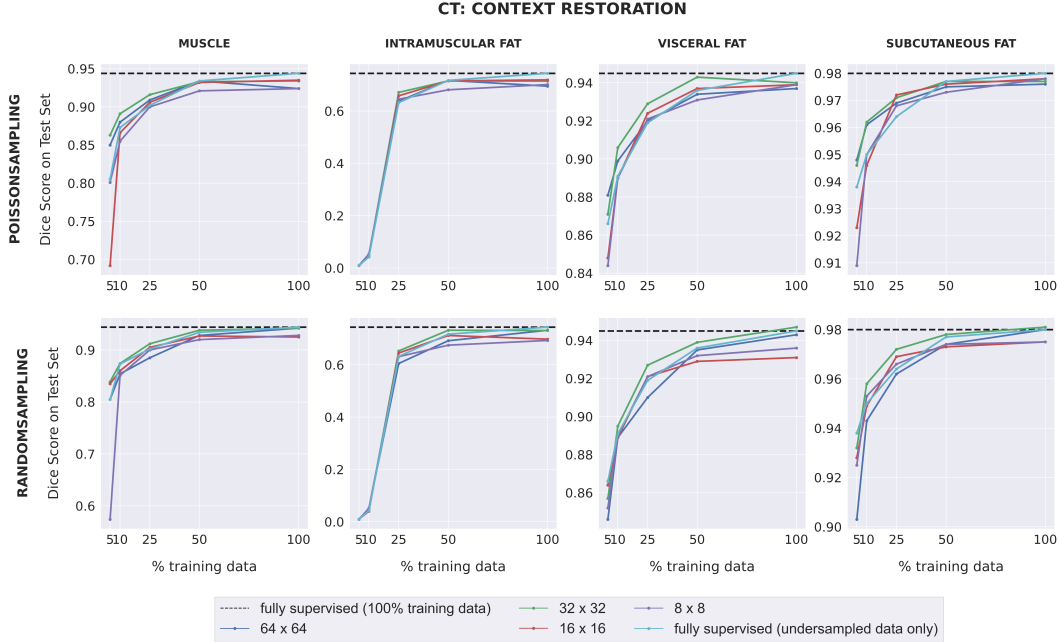


Figure 4: The downstream segmentation performance on the CT dataset for the Context Restoration pretext task as measured by the Dice score for every combination of patch size and sampling method used during pretraining, evaluated in five different scenarios of training data availability. In each scenario, every model is trained for segmentation using one of the five different subsets of training data as described in Section 2.1.2. The black dotted line in each plot indicates the performance of a fully supervised model trained using all available training images. The light blue curve indicates the performance of a fully supervised model when trained using each of the five different subsets of training data. Similar plots for the Context Prediction pretext task are given in the Supplementary Section.

training data, segmentation performances improved when the amount of pretraining data increased from 100% to 650%. There was limited improvement when the amount of pretraining data increased from 650% to 1200%.

Pretraining on the maximum amount of data enabled the optimally trained models to surpass the performance of fully supervised models for all extents of labeled training data, in both MRI and CT. For the MRI dataset, the highest improvement over supervised learning was observed when 5% labeled training data was used. For CT, considerable improvements over supervised learning were observed when 5%, 10%, or 25% labeled training data was used.

For both the MRI and CT datasets, the best average Dice score over all extents of labeled training data occurred when the maximum possible amount of pretraining data was used (200% pretraining data for MRI and 1200% pretraining data for CT).

3.5 Comparing SSL and Fully-Supervised Learning

For each dataset, optimally trained models were pretrained with the maximum amount of pretraining data from Section 3.4.

For all clinical metrics, using optimally trained models generally led to lower percent errors than using fully supervised models in regimes of 10% and 5% labeled training data (Figure 6). These differences were especially pronounced for CT tissue area, MRI tissue volume, and MRI mean T2 relaxation time. With 5% labeled training data for MRI, segmentations from optimally pretrained models more than halved the percent error for both tissue volume and mean T2 relaxation time of patellar cartilage, compared to segmentations from fully supervised models.

Table 2: Quantitative evaluation of inpainting for every combination of pretext task, patch size, and sampling method. All values are rounded to the nearest integer.

Pretext Task and Patch Size		MRI		CT	
		L2 Norm (mean \pm std)		L2 Norm (mean \pm std)	
Pretext Task	Patch Size	Poisson-Disc	Random	Poisson-Disc	Random
Context Prediction	64x64	94 \pm 9	105 \pm 9	123 \pm 13	134 \pm 18
	32x32	75 \pm 8	81 \pm 8	83 \pm 9	112 \pm 14
	16x16	61 \pm 7	64 \pm 7	66 \pm 8	74 \pm 10
	8x8	51 \pm 6	52 \pm 5	54 \pm 7	57 \pm 8
Context Restoration	64x64	96 \pm 9	116 \pm 11	142 \pm 19	346 \pm 158
	32x32	75 \pm 8	84 \pm 8	108 \pm 12	127 \pm 15
	16x16	62 \pm 7	67 \pm 7	86 \pm 10	93 \pm 12
	8x8	51 \pm 5	56 \pm 6	66 \pm 8	80 \pm 9

Table 3: Summary of the top five combinations of pretext tasks, patch sizes, and sampling methods for each dataset with the corresponding p-value for each combination, and sorted by p-value in ascending order. The bolded pretext task, patch size, and sampling method were chosen as the best combination of the three design choices.

MRI				
Rank	Pretext Task	Patch Size	Sampling Method	p-value
1	Context Restoration	64x64	Random	1.64×10^{-18}
2	Context Restoration	8x8	Random	1.89×10^{-18}
3	Context Restoration	32x32	Poisson-Disc	1.05×10^{-17}
4	Context Restoration	8x8	Poisson-Disc	4.03×10^{-17}
5	Context Restoration	32x32	Random	9.38×10^{-16}
CT				
Rank	Pretext Task	Patch Size	Sampling Method	p-value
1	Context Restoration	32x32	Poisson-Disc	6.29×10^{-17}
2	Context Restoration	64x64	Poisson-Disc	1.88×10^{-9}
3	Context Restoration	32x32	Random	4.12×10^{-7}
4	Context Prediction	64x64	Poisson-Disc	0.1
5	Context Prediction	64x64	Random	0.66

With 100% or 50% labeled training data, percent errors for all clinical metrics had lower improvement when optimally trained models were used. However, for MRI tissue volume, which requires accurate segmentation contours, optimally trained models almost always outperformed the fully supervised models, even in scenarios with large amounts of labeled training data.

For both datasets, clinical metrics improved the most for the most challenging classes to segment. This included intramuscular adipose tissue for CT, where percent error decreased from around 3940% to 3600% for tissue area when 10% labeled training data was used, and patellar cartilage for MRI, where percent error decreased from around 30% to 12% for tissue volume when 5% labeled training data was used.

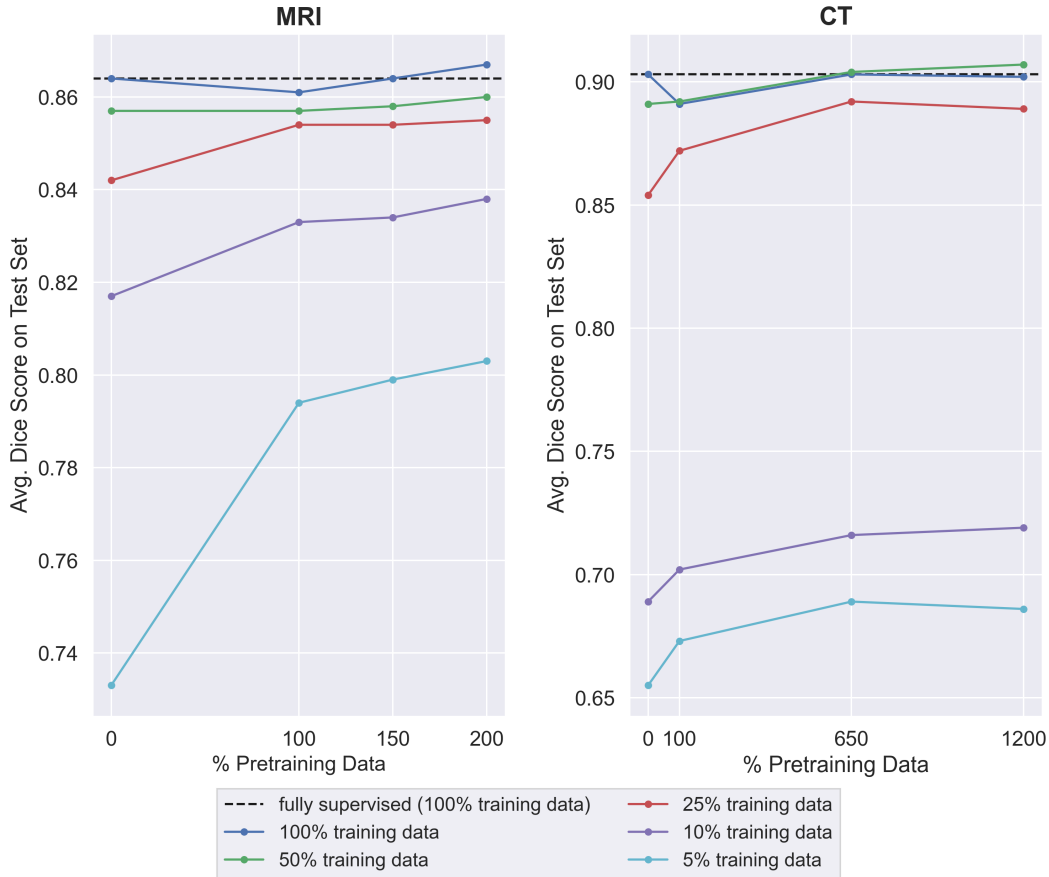


Figure 5: The downstream segmentation performance of the optimally trained model when pretrained with different amounts of pretraining data and fine-tuned using each of the five training data subsets. 100% pretraining data refers to the regular training set for each dataset. The data point for 0% pretraining data is the performance of a fully supervised model. The black dotted line indicates the performance of a fully supervised model trained on all available training data for the appropriate dataset.

4 Discussion

In this work, we investigated several key, yet under-explored design choices associated with pretraining and transfer learning in inpainting-based SSL for tissue segmentation. We examined the effect of inpainting-based SSL on the performance of tissue segmentation in various data and label regimes for MRI and CT scans, and compared it with fully supervised learning. We quantified performance using standard Dice scores and four clinically-relevant metrics of imaging biomarkers.

We observed that the crosstalk between the initial and fine-tuning learning rate was a design choice that most affected model performance. All model variants achieved optimal performance with an initial learning rate of $1e-3$ and a fine-tuning learning rate of $1e-4$ (Figure 7). This suggests the need for not perturbing the pretrained representations from the pretext task with a large learning rate. Moreover, although freezing and then fine-tuning the transferred weights provided an improvement over fine-tuning immediately for this learning rate combination (Figure 7), the improvement was very small. This result matches the findings of Kumar et al. [28], where the performance of linear probing (freezing) and then fine-tuning only slightly improved the performance of fine-tuning immediately after transferring. Additional details are provided in the Supplementary Material (Section 6.2.3).

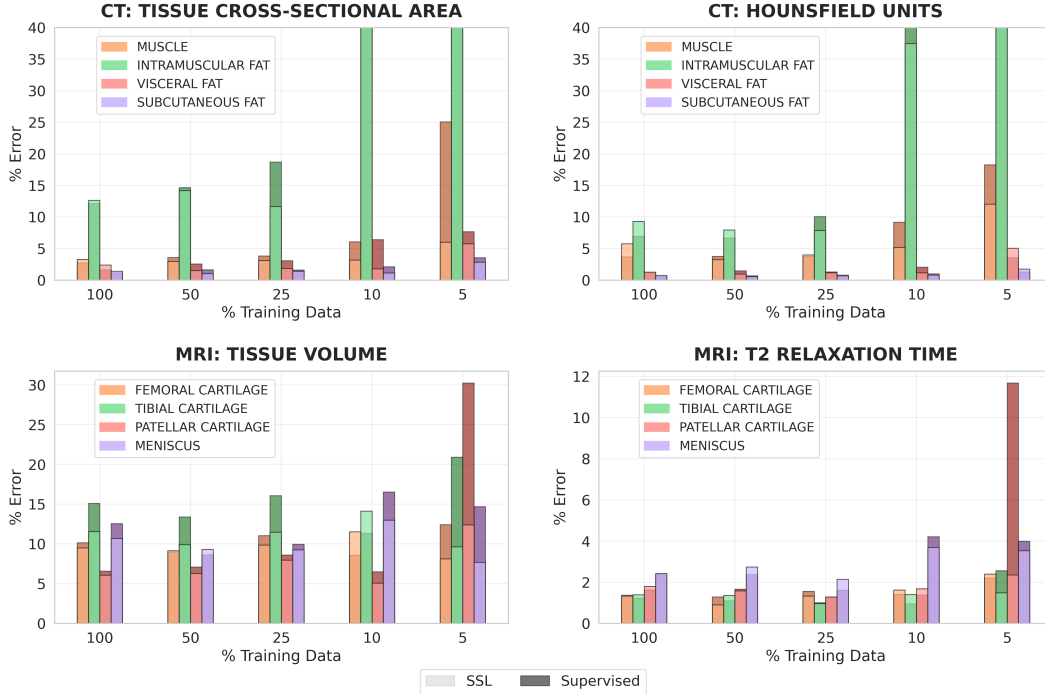


Figure 6: A comparison of the percent error in calculating clinical metrics for the MRI and CT datasets between when the tissue segmentations are generated by fully supervised models and when the tissue segmentations are generated by optimally trained models, pretrained using 200% data for MRI and 1200% data for CT. Each bar represents the median percent error across the test set for a particular tissue, clinical metric, and label regime. The percent error in the calculation of tissue area and mean HU for intramuscular fat extends beyond the limits of the y-axis when 10% and 5% labeled training data for segmentation is used.

Here, we suggest some best practices for inpainting-based SSL for medical imaging segmentation tasks. We observed that downstream segmentation performance for MRI was similar for all combinations of pretext tasks, patch sizes, and sampling techniques. This observation remained consistent despite significant differences in the L2 norms of the inpainted images. While decreasing patch sizes and sampling patch locations via Poisson-disc sampling to ensure non-overlapping patches both resulted in significantly lower L2 norms, they did not improve downstream segmentation performance. These observations suggest a discordance between learning semantically meaningful representations and the accuracy of the pretext task metric. Thus, simply performing *good enough* pretraining may be more important than optimizing pretext task performance.

For both MRI and CT, segmentation performance usually increased in proportion to the amount of pretraining data. The highest improvements over supervised learning were observed in the context of very low labeled data regimes of 5-25% labeled data. These empirical observations across both MRI and CT demonstrate that pretraining with large enough datasets improves performance compared to only supervised training, especially when the amount of available training data is limited.

Similar to supervised learning, improvements in SSL Dice scores tended to follow a power-law relationship as the size of the unlabeled corpora increased [4]. The observation that pretraining on 650% and 1200% CT pretraining data led to similar improvements over supervised learning suggests a limit exists where the learning capacity of a model saturates and additional unlabeled data may not improve downstream performance. A good practice for future segmentation studies may be to create Figure 5 to evaluate the trade-off between the challenges of annotating more images and acquiring more unlabeled images.

Compared to fully-supervised models, optimally trained models generally led to more accurate values for all clinical metrics in label-limited scenarios. We also observed that clinical metrics improved the most with SSL for tissue classes that had the highest percent error with fully supervised learning -

intramuscular adipose tissue in CT and patellar cartilage in MRI. This observation, combined with the Dice score improvement in low labeled data regimes, suggests that SSL may be most efficacious when the performance of the baseline fully supervised model is low.

When training with 5% labeled data for all MRI classes and muscle on CT, our optimal pretraining strategy improved Dice scores by over 0.05, compared to fully supervised learning. In such cases, the Dice score for fully supervised learning was 0.8 or lower, which suggests a critical performance threshold where inpainting-based SSL can improve segmentation performance over supervised learning. SSL may be beneficial in these cases because the models still have the capacity to learn more meaningful representations, compared to models with Dice scores over 0.8 that may already be saturated in their capacity to represent the underlying image.

Importantly, it should be noted that the improvement in segmentation performance with SSL pretraining in label-limited scenarios is on the similar order as prior advances that used complex DL architectures and training strategies [32, 33, 34]. Comparatively, our proposed SSL training paradigm offers an easy-to-use framework for improving model performance without requiring large and difficult to train DL models.

4.1 Study Limitations

There were a few limitations with this study. Although we investigated two different methods for selecting which pretrained weights to transfer, we did not conduct a systematic study across all possible choices due to computational constraints that made searching over the large search space too inefficient. We also leave other SSL strategies such as contrastive learning to future studies since it requires systematic evaluation of augmentations and sampling strategies. Furthermore, when we investigated the impact of unlabeled data extents on downstream segmentation performance, we did not pretrain our SSL models with equal extents of unlabeled MRI and CT data since we maximized the amount of available MRI data. Finally, our investigations in this work are limited to the U-Net architecture, though future work can explore other powerful segmentation architectures.

5 Conclusion

In this work, we investigated how inpainting-based SSL improves MRI and CT segmentation compared to fully-supervised learning, especially in label-limited regimes. We presented an optimized training strategy and open-source implementation for performing such pretraining. We describe the impact of pretraining task optimization and the relationship between the sizes of labeled and unlabeled training datasets. Our proposed approach for pretraining for improving segmentation performance that does not require additional manual annotation, complex model architectures, or model training techniques.

References

- [1] V. M. Campello, P. Gkontra, C. Izquierdo, C. Martín-Isla, A. Sojoudi, P. M. Full, K. Maier-Hein, Y. Zhang, Z. He, J. Ma *et al.*, “Multi-centre, multi-vendor and multi-disease cardiac segmentation: The m&ms challenge,” *IEEE Transactions on Medical Imaging*, 2021.
- [2] A. E. Kavur, N. S. Gezer, M. Barış, S. Aslan, P.-H. Conze, V. Groza, D. D. Pham, S. Chatterjee, P. Ernst, S. Özkan *et al.*, “Chaos challenge-combined (ct-mr) healthy abdominal organ segmentation,” *Medical Image Analysis*, vol. 69, p. 101950, 2021.
- [3] A. D. Desai, F. Caliva, C. Iriondo, A. Mortazi, S. Jambawalikar, U. Bagci, M. Perslev, C. Igel, E. B. Dam, S. Gaj *et al.*, “The international workshop on osteoarthritis imaging knee mri segmentation challenge: a multi-institute evaluation and analysis framework on a standardized dataset,” *Radiology: Artificial Intelligence*, vol. 3, no. 3, p. e200078, 2021.
- [4] A. D. Desai, G. E. Gold, B. A. Hargreaves, and A. S. Chaudhari, “Technical considerations for semantic segmentation in mri using convolutional neural networks,” *arXiv preprint arXiv:1902.01977*, 2019.
- [5] D. Pathak, P. Krahenbuhl, J. Donahue, T. Darrell, and A. A. Efros, “Context encoders: Feature learning by inpainting,” in *Proceedings of the IEEE conference on computer vision and pattern recognition*, 2016, pp. 2536–2544.

- [6] L. Chen, P. Bentley, K. Mori, K. Misawa, M. Fujiwara, and D. Rueckert, "Self-supervised learning for medical image analysis using image context restoration," *Medical image analysis*, vol. 58, p. 101539, 2019.
- [7] M. Noroozi and P. Favaro, "Unsupervised learning of visual representations by solving jigsaw puzzles," in *European conference on computer vision*. Springer, 2016, pp. 69–84.
- [8] L. Jing and Y. Tian, "Self-supervised visual feature learning with deep neural networks: A survey," *IEEE transactions on pattern analysis and machine intelligence*, vol. 43, no. 11, pp. 4037–4058, 2020.
- [9] K. Chaitanya, E. Erdil, N. Karani, and E. Konukoglu, "Contrastive learning of global and local features for medical image segmentation with limited annotations," *Advances in Neural Information Processing Systems*, vol. 33, 2020.
- [10] A. S. Chaudhari, F. Kogan, V. Padoia, S. Majumdar, G. E. Gold, and B. A. Hargreaves, "Rapid knee mri acquisition and analysis techniques for imaging osteoarthritis," *Journal of Magnetic Resonance Imaging*, vol. 52, no. 5, pp. 1321–1339, 2020. [Online]. Available: <https://onlinelibrary.wiley.com/doi/abs/10.1002/jmri.26991>
- [11] R. D. Boutin, D. K. Houston, A. S. Chaudhari, M. H. Willis, C. L. Fausett, and L. Lenchik, "Imaging of sarcopenia," *Radiologic Clinics*, vol. 60, no. 4, pp. 575–582, Jul 2022. [Online]. Available: <https://doi.org/10.1016/j.rcl.2022.03.001>
- [12] P. Goyal, D. Mahajan, A. Gupta, and I. Misra, "Scaling and benchmarking self-supervised visual representation learning," in *Proceedings of the IEEE/CVF International Conference on Computer Vision*, 2019, pp. 6391–6400.
- [13] A. D. Desai, A. M. Schmidt, E. B. Rubin, C. M. Sandino, M. S. Black, V. Mazzoli, K. J. Stevens, R. Boutin, C. Re, G. E. Gold *et al.*, "Sk-m-tea: A dataset for accelerated mri reconstruction with dense image labels for quantitative clinical evaluation," in *Thirty-fifth Conference on Neural Information Processing Systems Datasets and Benchmarks Track (Round 2)*, 2021.
- [14] A. S. Chaudhari, M. S. Black, S. Eijgenraam, W. Wirth, S. Maschek, B. Sveinsson, F. Eckstein, E. H. Oei, G. E. Gold, and B. A. Hargreaves, "Five-minute knee mri for simultaneous morphometry and t2 relaxometry of cartilage and meniscus and for semiquantitative radiological assessment using double-echo in steady-state at 3t," *Journal of Magnetic Resonance Imaging*, vol. 47, no. 5, pp. 1328–1341, 2018.
- [15] A. S. Chaudhari, K. J. Stevens, B. Sveinsson, J. P. Wood, C. F. Beaulieu, E. H. Oei, J. K. Rosenberg, F. Kogan, M. T. Alley, G. E. Gold, and B. A. Hargreaves, "Combined 5-minute double-echo in steady-state with separated echoes and 2-minute proton-density-weighted 2d FSE sequence for comprehensive whole-joint knee MRI assessment," *Journal of Magnetic Resonance Imaging*, vol. 49, no. 7, pp. e183–e194, Dec. 2018. [Online]. Available: <https://doi.org/10.1002/jmri.26582>
- [16] S. M. Eijgenraam, A. S. Chaudhari, M. Reijman, S. M. Bierma-Zeinstra, B. A. Hargreaves, J. Runhaar, F. W. Heijboer, G. E. Gold, and E. H. Oei, "Time-saving opportunities in knee osteoarthritis: T 2 mapping and structural imaging of the knee using a single 5-min mri scan," *European radiology*, vol. 30, no. 4, pp. 2231–2240, 2020.
- [17] A. S. Chaudhari, M. J. Grissom, Z. Fang, B. Sveinsson, J. H. Lee, G. E. Gold, B. A. Hargreaves, and K. J. Stevens, "Diagnostic accuracy of quantitative multicontrast 5-minute knee mri using prospective artificial intelligence image quality enhancement," *American Journal of Roentgenology*, vol. 216, no. 6, pp. 1614–1625, 2021.
- [18] J. M. Z. Chaves, A. S. Chaudhari, A. L. Wentland, A. D. Desai, I. Banerjee, R. D. Boutin, D. J. Maron, F. Rodriguez, A. T. Sandhu, R. B. Jeffrey *et al.*, "Opportunistic assessment of ischemic heart disease risk using abdominopelvic computed tomography and medical record data: a multimodal explainable artificial intelligence approach," *medRxiv*, 2021.
- [19] O. Ronneberger, P. Fischer, and T. Brox, "U-net: Convolutional networks for biomedical image segmentation," in *International Conference on Medical image computing and computer-assisted intervention*. Springer, 2015, pp. 234–241.
- [20] Y. Wu and K. He, "Group normalization," in *Proceedings of the European conference on computer vision (ECCV)*, 2018, pp. 3–19.

- [21] S. Qiao, H. Wang, C. Liu, W. Shen, and A. Yuille, “Micro-batch training with batch-channel normalization and weight standardization,” *arXiv preprint arXiv:1903.10520*, 2019.
- [22] K. He, X. Zhang, S. Ren, and J. Sun, “Delving deep into rectifiers: Surpassing human-level performance on imagenet classification,” in *Proceedings of the IEEE international conference on computer vision*, 2015, pp. 1026–1034.
- [23] D. P. Kingma and J. Ba, “Adam: A method for stochastic optimization,” *arXiv preprint arXiv:1412.6980*, 2014.
- [24] R. Geirhos, J.-H. Jacobsen, C. Michaelis, R. Zemel, W. Brendel, M. Bethge, and F. A. Wichmann, “Shortcut learning in deep neural networks,” *Nature Machine Intelligence*, vol. 2, no. 11, pp. 665–673, 2020.
- [25] S. Kornblith, J. Shlens, and Q. V. Le, “Do better imagenet models transfer better?” in *Proceedings of the IEEE/CVF conference on computer vision and pattern recognition*, 2019, pp. 2661–2671.
- [26] A. Newell and J. Deng, “How useful is self-supervised pretraining for visual tasks?” in *Proceedings of the IEEE/CVF Conference on Computer Vision and Pattern Recognition*, 2020, pp. 7345–7354.
- [27] A. Park, C. Chute, P. Rajpurkar, J. Lou, R. L. Ball, K. Shpanskaya, R. Jabarkheel, L. H. Kim, E. McKenna, J. Tseng *et al.*, “Deep learning–assisted diagnosis of cerebral aneurysms using the headxnet model,” *JAMA network open*, vol. 2, no. 6, pp. e195 600–e195 600, 2019.
- [28] A. Kumar, A. Raghunathan, R. Jones, T. Ma, and P. Liang, “Fine-tuning can distort pretrained features and underperform out-of-distribution,” *arXiv preprint arXiv:2202.10054*, 2022.
- [29] R. Bridson, “Fast poisson disk sampling in arbitrary dimensions.” *SIGGRAPH sketches*, vol. 10, no. 1, 2007.
- [30] B. Sveinsson, A. Chaudhari, G. Gold, and B. Hargreaves, “A simple analytic method for estimating t2 in the knee from DESS,” *Magnetic Resonance Imaging*, vol. 38, pp. 63–70, May 2017. [Online]. Available: <https://doi.org/10.1016/j.mri.2016.12.018>
- [31] P. Virtanen, R. Gommers, T. E. Oliphant, M. Haberland, T. Reddy, D. Cournapeau, E. Burovski, P. Peterson, W. Weckesser, J. Bright *et al.*, “Scipy 1.0: fundamental algorithms for scientific computing in python,” *Nature methods*, vol. 17, no. 3, pp. 261–272, 2020.
- [32] W. Dai, B. Woo, S. Liu, M. Marques, F. Tang, S. Crozier, C. Engstrom, and S. Chandra, “Can3d: Fast 3d knee mri segmentation via compact context aggregation,” in *2021 IEEE 18th International Symposium on Biomedical Imaging (ISBI)*. IEEE, 2021, pp. 1505–1508.
- [33] M. Perslev, A. Pai, J. Runhaar, C. Igel, and E. B. Dam, “Cross-cohort automatic knee mri segmentation with multi-planar u-nets,” *Journal of Magnetic Resonance Imaging*, 2021.
- [34] E. Panfilov, A. Tiulpin, S. Klein, M. T. Nieminen, and S. Saarakkala, “Improving robustness of deep learning based knee mri segmentation: Mixup and adversarial domain adaptation,” in *Proceedings of the IEEE/CVF International Conference on Computer Vision Workshops*, 2019, pp. 0–0.
- [35] L. Prechelt, “Early stopping-but when?” in *Neural Networks: Tricks of the trade*. Springer, 1998, pp. 55–69.
- [36] F. Chollet *et al.*, “Keras,” <https://keras.io>, 2015.
- [37] M. Abadi, A. Agarwal, P. Barham, E. Brevdo, Z. Chen, C. Citro, G. S. Corrado, A. Davis, J. Dean, M. Devin, S. Ghemawat, I. Goodfellow, A. Harp, G. Irving, M. Isard, Y. Jia, R. Jozefowicz, L. Kaiser, M. Kudlur, J. Levenberg, D. Mané, R. Monga, S. Moore, D. Murray, C. Olah, M. Schuster, J. Shlens, B. Steiner, I. Sutskever, K. Talwar, P. Tucker, V. Vanhoucke, V. Vasudevan, F. Viégas, O. Vinyals, P. Warden, M. Wattenberg, M. Wicke, Y. Yu, and X. Zheng, “TensorFlow: Large-scale machine learning on heterogeneous systems,” 2015, software available from tensorflow.org. [Online]. Available: <https://www.tensorflow.org/>

6 Supplementary Material

6.1 Implementation Details

6.1.1 Model Architecture and Optimization

The loss function for inpainting was the L2 loss, implemented as in Equation 1 for a model output (X) and ground truth (Y), where N , H , W , and C denote the batch size, height, width, and number of channels of the images, respectively.

$$L_{inpainting}(X, Y) = \frac{1}{C} \sum_{c=0}^{C-1} \frac{1}{N} \sum_{n=0}^{N-1} \sum_{h=0}^{H-1} \sum_{w=0}^{W-1} (X_{n,h,w,c} - Y_{n,h,w,c})^2 \quad (1)$$

The loss function for segmentation was a variant of the Dice loss, implemented as in Equation 2 for a model output (X) and ground truth (Y), where N , H , W , and C denote the batch size, height, width, and number of channels of the images, respectively. Due to the instability of pixel-wise losses for sparse classes, we used a batch-aggregate Dice loss, where the Dice loss was computed over the aggregate of a mini-batch per segmentation class and the final loss was the mean Dice loss across segmentation classes.

$$L_{segmentation}(X, Y) = \frac{1}{C} \sum_{c=0}^{C-1} 1 - \frac{2 * \sum_{n=0}^{N-1} \sum_{h=0}^{H-1} \sum_{w=0}^{W-1} (X_{n,h,w,c} * Y_{n,h,w,c}) + \epsilon}{\sum_{n=0}^{N-1} \sum_{h=0}^{H-1} \sum_{w=0}^{W-1} (X_{n,h,w,c} + Y_{n,h,w,c}) + \epsilon} \quad (2)$$

For inpainting, the learning rate was set to 1e-3 and decayed by a factor of 0.9 every 2 epochs. To prevent overfitting, early stopping [35] based on the validation L2 loss was used with a threshold of 50 and patience of 4 epochs. For a baseline fully-supervised segmentation, the learning rate followed the same schedule as inpainting. For self-supervised segmentation, the fine-tuning learning rate was considered a design choice and is described in Section 2.5.1. For both fully-supervised and self-supervised segmentation, early stopping based on the validation Dice loss was used to prevent overfitting, with a threshold of 1e-3 and a patience of 10 epochs. All inpainting and segmentation models were trained until the criteria for early stopping was achieved. The same random seed was used for all experiments.

All models were trained using the Keras (v2.1.6) software library [36], with Tensorflow (v1.15.0) [37] as the backend.

6.1.2 Design Choices for SSL Implementation

For all experiments described in Section 2.5, the self-supervised models were pretrained on all of the training data for the appropriate dataset.

6.2 Design Choices for Transfer Learning

6.2.1 Grid Search Implementation

As described in Section 2.5.1, we compared two methods for selecting which pretrained weights to transfer and two methods for fine-tuning the transferred pretrained weights. To compare the four combinations of these two design choices, we trained one model per combination. Since the first fine-tuning method, in which the pretrained weights are fine-tuned immediately, involves one training run, and the second fine-tuning method, in which the pretrained weights are first frozen, involves two training runs, we chose to train the two models in which the pretrained weights were fine-tuned immediately two times to ensure a fair comparison.

To investigate the impact of the initial learning rate during fine-tuning, we trained each of the four models four times during the first training run, each time with one of the four possible initial learning rates, and then trained each of the sixteen trained models again four times, each time with one of the four possible initial learning rates.

We selected the learning rates 1e-2, 1e-3, 1e-4, and 1e-5 for specific reasons. 1e-2 was selected as an example of a large learning rate, to determine if fine-tuning with a large learning rate will destroy pretrained features. 1e-3 was selected as an example of a "common" learning rate, and was used as the initial learning rate for all our other experiments. Finally, 1e-4 and 1e-5 were selected arbitrarily as examples of small learning rates.

All pretrained weights were derived from an inpainting model that was trained with context prediction with 16x16 patches and Poisson-disc sampling, and all models were fine-tuned for segmentation using the MRI training subset with 5% data. The same random seed was used when training each model. All models were compared by computing the Dice coefficient for each volume in the MRI test set, averaged across the four segmentation classes.

6.2.2 Results

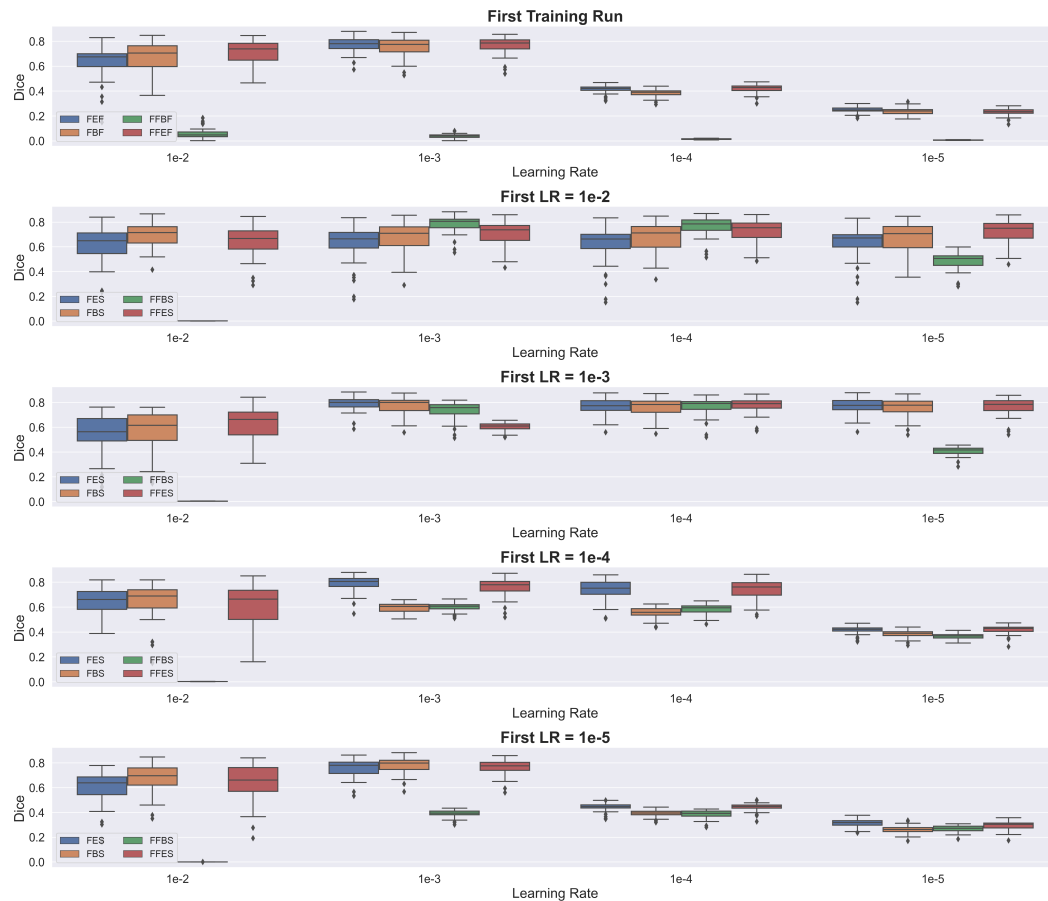


Figure 7: Box plots displaying the spread of Dice scores among the volumes in the MRI test set. The top row displays the spread of Dice scores after each type of model was trained once, with the initial learning rate set to the appropriate value on the x-axis. The remaining four rows display the spread of Dice scores after each model in the first row was trained again, with the initial learning rate set to the appropriate value on the x-axis. We used the following structure for acronyms to distinguish between the different types of models: **ABC**. If **A** is F, the pretrained weights were fine-tuned immediately, and if **A** is FF, the pretrained weights were first frozen and then fine-tuned. If **B** is E, only the pretrained encoder weights were transferred, and if **B** is B, both the pretrained encoder and decoder weights were transferred. If **C** is F, the model was trained only once (the first training run), and if **C** is S, the model was trained a second time (the second training run).

For the first training run following pretraining, higher initial learning rates of 1e-2 and 1e-3 produced better results. The FEF, FBF, and FFES models had similar performance for all initial learning rates, and consistently performed better than the FFBF models (Figure 7).

When each type of model was trained for a second time with an initial learning rate of $1e-2$, each model's performance was similar to its performance when trained only once with an initial learning rate of $1e-2$. This occurred regardless of the initial learning rate during the first training run. For example, the FEF, FBF, and FFEF models had relatively high performance when trained once with an initial learning rate of $1e-3$, but when these models were trained for a second time with an initial learning rate of $1e-2$, the performance of all three models dropped to the same level of performance as when each type of model was trained only once with an initial learning rate of $1e-2$. Similarly, but in the opposite way, the FEF, FBF, and FFEF models had relatively low performance when trained once with an initial learning rate of $1e-4$ or $1e-5$, but when these models were trained for a second time with an initial learning rate of $1e-2$, the performance of all three models increased to the same level of performance as when each type of model was trained only once with an initial learning rate of $1e-2$.

When each type of model was trained once with an initial learning rate of $1e-2$ and then trained a second time with a smaller learning rate, the FFBS models outperformed the FES and FBS models when the initial learning rate of the second training run was $1e-3$ or $1e-4$, and the FFES models outperformed the FES and FBS models for all initial learning rates smaller than $1e-2$.

When each type of model was trained once with an initial learning rate of $1e-4$ and then trained a second time with an initial learning rate of $1e-3$ or lower, the FES and FFES models had similar performance and always outperformed the FBS and FFBS models.

When each type of model was trained once with an initial learning rate of $1e-3$, training each model again with an initial learning rate equal to or less than $1e-3$ did not improve or only slightly improved the model's performance. The exception was the FFBF model, for which the performance always increased by a large amount during the second training run, regardless of the initial learning rate used during the second training run. The FEF, FES, FBF, and FBS models had similar performance when the initial learning rates for the first and second training runs were set to $1e-3$.

We concluded that FEF (fine-tuning immediately after transferring only the pretrained encoder weights), trained with an initial learning rate of $1e-3$, was the best combination of design choices for transfer learning because this model achieved high segmentation performance with minimal training time.

6.2.3 Discussion

In this experiment, we determined the best combination of fine-tuning mechanism, weight loading strategy, and initial learning rate during fine-tuning. Overall, every model had high performance when first trained with an initial learning rate of $1e-3$ and then trained a second time with an initial learning rate of $1e-4$, despite using different fine-tuning mechanisms and different methods for selecting which pretrained weights to transfer. This suggests choosing the initial learning rates for the first and second training runs is the design choice for transfer learning that most affects model performance.

If the initial learning rate of the first training run is too large, like $1e-2$, the pretrained features are at risk of being destroyed. For example, the FEF and FBF models performed worse when trained with an initial learning rate of $1e-2$ than when trained with an initial learning rate of $1e-3$. Furthermore, when the initial learning rate during the second training run is too large, a model has a risk of escaping out of an already found local minimum. For example, although the FBF model had high performance when trained once with an initial learning rate of $1e-3$, its performance dropped when trained again with an initial learning rate of $1e-2$.

On the other hand, if the initial learning rate is too small, a model may not be able to learn during fine-tuning. This was suggested by the low performance of all four types of models when they were trained once with an initial learning rate of $1e-5$ and then trained again with an initial learning rate of either $1e-4$ or $1e-5$.

Although the design choice for transfer learning that most affects model performance is the initial learning rate during fine-tuning, the results of this experiment suggest that transferring only the pretrained encoder weights may lead to better performance gains than transferring both the pretrained encoder and decoder weights. For instance, in the first training run, the FFEF models performed similarly to the FEF models for all initial learning rates, suggesting the frozen encoder features in the FFEF models were as good as the fine-tuned encoder features in the FEF models. In addition, when the four types of models were first trained with an initial learning rate of $1e-4$ and then trained again with an initial learning rate of $1e-3$ or lower, the FES and FFES models always outperformed the

FBS and FFBS models. These results suggest that transferring only the pretrained encoder weights provides a better initialization point for segmentation fine-tuning than transferring both the pretrained encoder and decoder weights.

6.3 Design Choices for Pretraining: Supplementary Figures

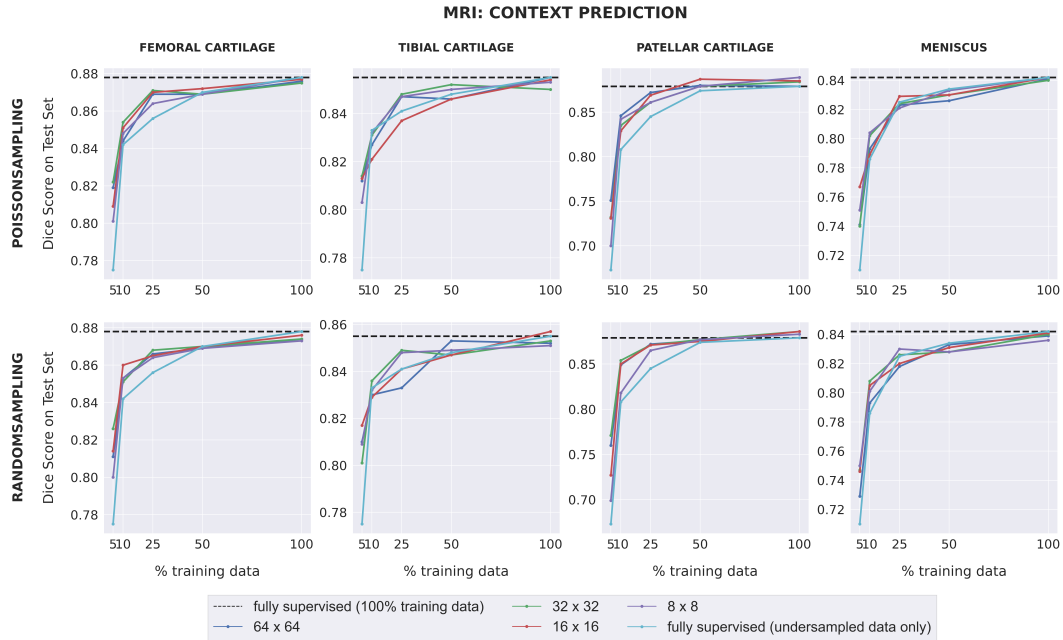


Figure 8: The downstream segmentation performance on the MRI dataset for the Context Prediction pretext task as measured by the Dice score for every combination of patch size and sampling method used during pretraining, evaluated in five different scenarios of training data availability. In each scenario, every model is trained for segmentation using one of the five different subsets of training data as described in Section 2.1.1. The black dotted line in each plot indicates the performance of a fully supervised model trained using all available training images. The light blue curve indicates the performance of a fully supervised model when trained using each of the five different subsets of training data.

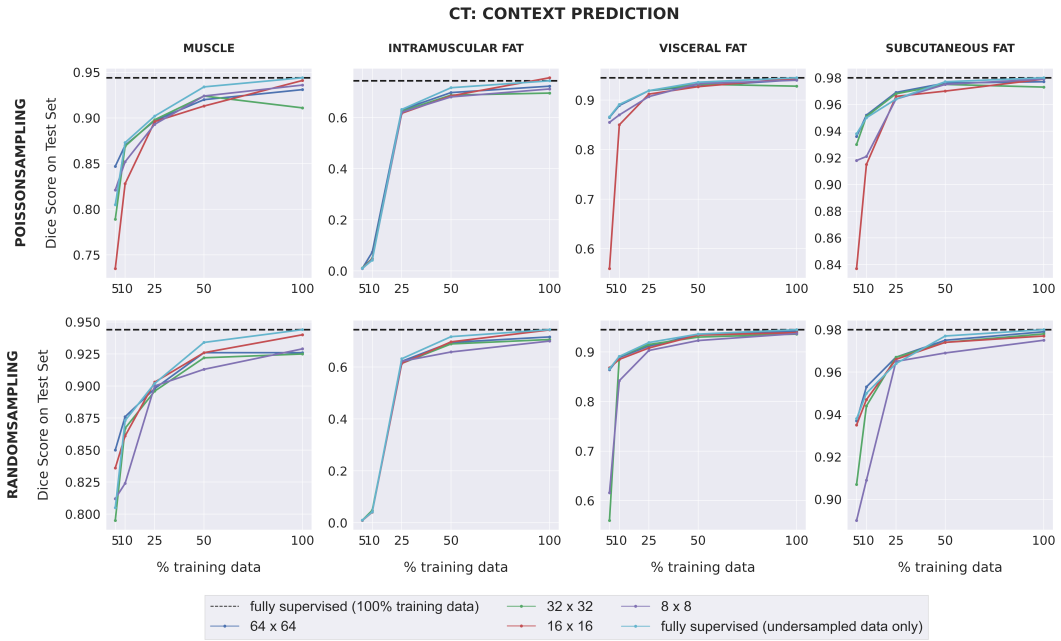


Figure 9: The downstream segmentation performance on the CT dataset for the Context Prediction pretext task as measured by the Dice score for every combination of patch size and sampling method used during pretraining, evaluated in five different scenarios of training data availability. In each scenario, every model is trained for segmentation using one of the five different subsets of training data as described in Section 2.1.2. The black dotted line in each plot indicates the performance of a fully supervised model trained using all available training images. The light blue curve indicates the performance of a fully supervised model when trained using each of the five different subsets of training data.